The Astrophysical Journal, 923:137 (10pp), 2021 December 20 https://doi.org/10.3847/1538-4357/ac2c73

How Identifying Circumgalactic Gas by Line-of-sight Velocity instead of the Location in 3D Space Affects O VI Measurements

Stephanie H. Ho[1,2], Crystal L. Martin[3], and Joop Schaye[4]
[1] George P. and Cynthia Woods Mitchell Institute for Fundamental Physics and Astronomy, Texas A&M University, College Station, TX 77843-4242, USA
shho@physics.tamu.edu
[2] Department of Physics and Astronomy, Texas A&M University, College Station, TX 77843-4242, USA
[3] Department of Physics, University of California, Santa Barbara, CA 93106, USA
[4] Leiden Observatory, Leiden University, P.O. Box 9513, 2300 RA, Leiden, The Netherlands
Received 2021 July 4; revised 2021 September 30; accepted 2021 October 1; published 2021 December 16

Abstract

The high incidence rate of the O VI $\lambda\lambda$1032, 1038 absorption around low-redshift, $\sim L^*$ star-forming galaxies has generated interest in studies of the circumgalactic medium. We use the high-resolution EAGLE cosmological simulation to analyze the circumgalactic O VI gas around $z \approx 0.3$ star-forming galaxies. Motivated by the limitation that observations do not reveal where the gas lies along the line of sight, we compare the O VI measurements produced by gas within fixed distances around galaxies and by gas selected using line-of-sight velocity cuts commonly adopted by observers. We show that gas selected by a velocity cut of ± 300 km s^{-1} or ± 500 km s^{-1} produces a higher O VI column density, a flatter column density profile, and a higher covering fraction compared to gas within 1, 2, or 3 times the virial radius ($r_{\rm vir}$) of galaxies. The discrepancy increases with impact parameter and worsens for lower-mass galaxies. For example, compared to the gas within 2 $r_{\rm vir}$, identifying the gas using velocity cuts of 200–500 km s^{-1} increases the O VI column density by 0.2 dex (0.1 dex) at 1 $r_{\rm vir}$ to over 0.75 dex (0.7 dex) at ≈ 2 $r_{\rm vir}$ for galaxies with stellar masses of 10^9–$10^{9.5}$ $M_\odot$ (10^{10}–$10^{10.5}$ $M_\odot$). We furthermore estimate that excluding O VI outside $r_{\rm vir}$ decreases the circumgalactic oxygen mass measured by Tumlinson et al. (2011) by over 50%. Our results demonstrate that gas at large line-of-sight separations but selected by conventional velocity windows has significant effects on the O VI measurements and may not be observationally distinguishable from gas near the galaxies.

Unified Astronomy Thesaurus concepts: Circumgalactic medium (1879); Extragalactic astronomy (506); Hydrodynamical simulations (767)

1. Introduction

Absorption-line spectroscopy has revealed the substantial reservoir of baryons and metals surrounding galaxies, known as the circumgalactic medium (CGM; Tumlinson et al. 2017, and references therein). The CGM extends to at least the virial radius $r_{\rm vir}$ and regulates the interplay between the gas accretion onto galaxies and the feedback from massive stars. The ubiquitous detection of the O VI$\lambda\lambda$1032, 1038 absorption in sightlines intersecting the CGM of $\sim L^*$ star-forming galaxies in contrast to the rare O VI detection around quiescent galaxies has drawn particular attention (Tumlinson et al. 2011). This observed "O VI bimodality" possibly indicates a link between O VI and ongoing star formation. This link may however be indirect. The absence of detectable O VI may indicate lower CGM mass fractions, which in turn may result from active galactic nucleus (AGN) feedback (Nelson et al. 2018; Davies et al. 2020), or higher virial temperatures and hence halo masses (Oppenheimer et al. 2016).

Dedicated observational efforts have characterized the circumgalactic O VI properties and explored its dependence on galaxy properties and its relationship with the low-ionization-state (LIS) absorbers (e.g., Mg II, Si II). The $\sim L^*$ star-forming galaxies do not only have a higher O VI incidence rate and column density than quiescent galaxies (Tumlinson et al. 2011) but also compared with dwarf galaxies (Prochaska et al. 2011; Johnson et al. 2015, 2017) and massive luminous red galaxies (Zahedy et al. 2019). This suggests that the strength of the O VI absorption depends on star formation and/or the galaxy mass. The O VI column density decreases with the sightline impact parameter, but the decline is less steep (Tumlinson et al. 2011; Stern et al. 2018) compared to the LIS absorbers (Chen et al. 2010; Huang et al. 2021). Even though O VI systems have broader line profiles than the LIS counterparts (Werk et al. 2016; Nielsen et al. 2017), most O VI absorption components have matching LIS components with similar Doppler shifts (Werk et al. 2016). However, unlike the tentative evidence for stronger and broader LIS absorption detected near the galaxy minor axes compared to that near the galaxy major axes (Kacprzak et al. 2012; Nielsen et al. 2015), a result typically attributed to galactic outflows (Martin et al. 2019; Schroetter et al. 2019), O VI absorption is kinematically uniform at all azimuthal angles (Nielsen et al. 2017).[5] The O VI Doppler shifts measured in major-axis sightlines do not correlate with disk rotation (Kacprzak et al. 2019), whereas the LIS gas corotates with the galaxy (Ho et al. 2017; Zabl et al. 2019; Ho & Martin 2020). These similarities and differences in the low ions and O VI properties highlight the complexity of the multiphase CGM.

One challenge for interpreting the observed circumgalactic absorption, is that absorption-line measurements do not reveal where the gas lies along the line of sight (LOS). Observers typically associate the absorbing gas with the galaxy at the smallest impact parameter from the sightline that has a comparable redshift, i.e., within a preset line-of-sight velocity window from the galaxy systemic velocity. However, the gas

[5] The azimuthal angle is the angle between the galaxy major axis and the line joining the sightline and the center of the galaxy.

potentially resides relatively far away from the galaxy in 3D space and may therefore have no direct physical relation with the galaxy (see Ho et al. 2020 for a study of this issue for Mg II absorption). Faint galaxies responsible for the absorption may also remain undetected until deeper imaging and spectroscopy of the galaxy field becomes available, and incorrectly associating the gas to another bright galaxy in the field would alter the interpretation of the origin of the detected gas. These uncertainties in identifying the gas associated with target galaxies lead to possible errors in interpreting the CGM properties from absorption-line measurements.

The ambiguity of the relative location between the gas and the galaxies does not pose a problem for CGM analyses using large volume hydrodynamic simulations, though zoom-in simulations may underestimate the projection effects. Simulations that reproduce the radial profiles of the column density of LIS gas (Ford et al. 2016; Oppenheimer et al. 2018a) often underestimate the O VI column density around $\sim L^*$ galaxies by about a factor of 2 (e.g., Hummels et al. 2013; Oppenheimer et al. 2016; Gutcke et al. 2017; Suresh et al. 2017; Marra et al. 2021). This problem could potentially be resolved by fossil AGN proximity zones (Oppenheimer & Schaye 2013; Oppenheimer et al. 2018b), by black hole feedback (Nelson et al. 2018), by including cosmic-ray physics (Ji et al. 2020), or by changing the model for the UV background (Appleby et al. 2021). While simulations reproduced the O VI bimodality observed in the star-forming and quiescent galaxy sample from Tumlinson et al. (2011) (Oppenheimer et al. 2016; Nelson et al. 2018), Oppenheimer et al. (2016) suggested that the observed bimodality was due to the higher halo mass of the quiescent galaxy sample; the virial temperature of the $\sim L^*$ star-forming galaxies ($\sim 10^{5.5}$ K) coincides with the narrow temperature range at which the O VI fraction peaks in a collisionally ionized plasma.

This paper focuses on the circumgalactic O VI gas using the high-resolution EAGLE simulation (Crain et al. 2015; Schaye et al. 2015). EAGLE broadly reproduces many galaxy observables, e.g., the galaxy stellar mass function (Schaye et al. 2015), the evolution of galaxy masses (Furlong et al. 2015), sizes (Furlong et al. 2017), colors (Trayford et al. 2015, 2017), and gas contents (Lagos et al. 2015; Bahé et al. 2016; Crain et al. 2017). Although EAGLE was not calibrated to match the observed CGM properties, the simulation shows broad agreement with absorption-line statistics for both H I and metal ions (Rahmati et al. 2015, 2016; Turner et al. 2016, 2017; Oppenheimer et al. 2018a). For example, EAGLE reproduces the anticorrelation between the covering fraction and impact parameter of low ions (Oppenheimer et al. 2018a) and the observed O VI bimodality in low-redshift galaxies (Oppenheimer et al. 2016).

In this paper, we analyze the O VI gas around low-redshift galaxies and focus on how selecting the gas around galaxies by LOS velocity instead of 3D distance affects the O VI measurements and the interpretations of the O VI properties of galaxies. We present the paper as follows. Section 2 describes the EAGLE simulation. In Section 3, we present the O VI measurements and contrast the results from gas selected using different fixed radii and LOS velocity windows. We discuss the observational consequences and conclude in Section 4. Throughout this paper, we use the flat ΛCDM cosmology with $(\Omega_m, \Omega_\Lambda, h) = (0.307, 0.693, 0.6777)$ adopted by EAGLE from Planck Collaboration et al. (2014). We prefix comoving and proper (i.e., physical) length units with "c" and "p," respectively, e.g., cMpc and pkpc.

2. Galaxy Selection in the EAGLE Simulation and Column Density Maps

2.1. Simulation Overview and Galaxy Selection

The EAGLE simulation suite consists of a large number of cosmological hydrodynamical simulations with different resolutions, cosmological volumes, and physical models (Crain et al. 2015; Schaye et al. 2015; McAlpine et al. 2016). EAGLE was performed using a modified version of the *N*-Body Tree-PM smoothed particle hydrodynamics (SPH) code GADGET-3 (last described in Springel 2005) with a new hydrodynamics solver (Schaller et al. 2015). Unresolved physical processes are captured by state-of-the-art subgrid models, including radiative cooling and photoheating, star formation, stellar evolution and enrichment, stellar feedback, and black hole growth and AGN feedback. Schaye et al. (2015) introduced a reference model; the subgrid model parameters for energy feedback from stars and accreting black holes were calibrated to reproduce the $z \approx 0$ galaxy stellar mass function, the sizes of disk galaxies, and the amplitude of the galaxy–central black hole mass relation.

EAGLE defines galaxies using the SUBFIND algorithm (Springel et al. 2001; Dolag et al. 2009). Briefly, the friends-of-friends (FoF) algorithm connects dark matter particles to the same halo if the particle separation is below 0.2 times the average particle separation. Baryons are linked to the same halo (if it exists) as their closest dark matter particle. In each FoF halo, SUBFIND identifies self-bound overdense regions as subhalos. Each subhalo represents a galaxy. The central galaxy is defined as the subhalo with the particle at the lowest gravitational potential, and the location of this particle represents the center of the central galaxy.

In this work, we use the Recal-L0025N0752 simulation with a box size of 25 cMpc.[6] This simulation has a dark matter particle mass of $1.21 \times 10^6\ M_\odot$, an initial baryonic particle mass of $2.26 \times 10^5\ M_\odot$, and a Plummer-equivalent gravitational softening length of 0.35 pkpc at the low redshift we study here. This simulation run has 8 (2) times better mass (spatial) resolution compared to the default EAGLE intermediate-resolution runs (e.g., Ref-L0100N1504). We analyze the $z = 0.271$ snapshot output[7]; this redshift is comparable to the redshifts of targeted galaxies in circumgalactic O VI observations (e.g., Tumlinson et al. 2011; Johnson et al. 2015, 2017; Kacprzak et al. 2019; Beckett et al. 2021). Because EAGLE applied periodic boundary conditions, the maximum LOS separation is half of the box size and corresponds to a velocity difference of 767 km s^{-1} (physical) at $z = 0.271$.

We select central, star-forming galaxies with stellar masses ($M_\star$) between 10^9 to $10^{11}\ M_\odot$. The galaxy stellar mass is defined as the total mass of star particles associated with the subhalo within 30 pkpc (in 3D) from the galaxy center (Schaye et al. 2015). Following Ho et al. (2020), galaxies are classified as star-forming if they lie above the dividing line between star-forming and quiescent galaxies on the SFR–$M_\star$ plane as

[6] The "Recal" model was calibrated to the same $z \approx 0$ galaxy properties as the reference model, but subgrid parameters for stellar and AGN feedback were modified and recalibrated as a consequence of the higher resolution compared to the default (intermediate) resolution runs.

[7] Particle data snapshots can be downloaded from http://icc.dur.ac.uk/Eagle/database.php.

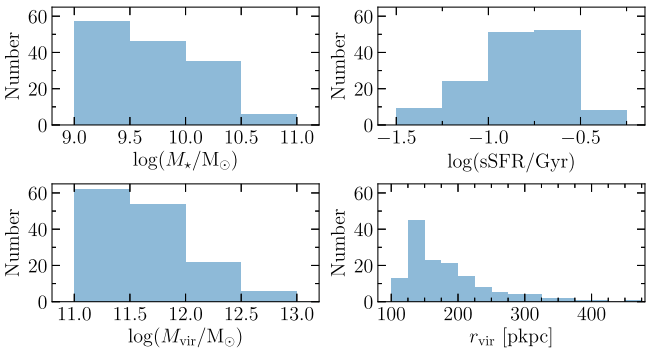

Figure 1. Distributions of stellar mass $M_\star$, specific star formation rate (sSFR), halo virial mass $M_{\rm vir}$, and virial radius $r_{\rm vir}$ of the selected central, star-forming galaxies. The sample consists of 144 star-forming galaxies.

defined by Moustakas et al. (2013), who fitted a redshift-dependent relation to separate star-forming and quiescent galaxies using ∼120,000 spectroscopically observed galaxies in the PRism MUlti-object Survey (also see Figure 1 of Ho et al. 2020). Our sample consists of 144 star-forming galaxies; Figure 1 shows the distributions of the galaxy stellar mass, specific star formation rate, halo virial mass, and virial radius of the sample.[8]

2.2. Column Density Maps

We project galaxies along the z-axis in the simulation box and produce the O VI (and Mg II) column density maps. Calculating the ionic column density requires the element abundance and the ion fraction, i.e., the number of atoms in each ionization state divided by the total number of atoms of the element in the gas phase. For O VI we use the ion fraction tables from Bertone et al. (2010a, 2010b), who adopted the UV/X-ray background by Haardt & Madau (2001) and computed the tables under the same assumptions as the gas cooling in the EAGLE runs. For Mg II we obtain the ion fraction using the fiducial model in Ploeckinger & Schaye (2020), whose calculations use the UV/X-ray background by Faucher-Giguère (2020) [9] and include the effects of depletion of metals onto dust grains and self-shielding (also see Ho et al. 2020). The Mg II fraction will be slightly different compared to that used for computing the cooling rates during the EAGLE run, because EAGLE used a different UV background model and did not include self-shielding. However, we do not expect the difference to be significant, because magnesium is not an important coolant (Wiersma et al. 2009). We interpolate the ion fraction tables in redshift, log temperature, and log density to obtain the O VI and Mg II ion fractions per SPH particle. Then we multiply the ion fraction by the particle mass and the element abundance to calculate the number of ions per particle. We obtain the column density by summing the total number of ions through a gas column and divide that by the cross-sectional area of the column, during which the spatial distribution of gas (i.e., the ion) of each SPH particle is modeled by the same C^2 Wendland (1995) kernel used for the hydrodynamics calculations in the EAGLE simulations (also see Wijers et al. 2019). For our galaxies, Mg II traces $T\sim10^4$ K gas and is photoionized, whereas collisionally ionized O VI ($T\approx10^{5.5}$ K) dominates the inner radius. Photoionized O VI becomes increasingly important at larger radii especially for lower-mass galaxies (with $T\lesssim10^5$ K and density $n_H\lesssim10^{-4.5}$ cm^{-3}). This agrees with the radial and galaxy mass dependence of O VI ionization shown in recent work from zoom-in simulations (Roca-Fàbrega et al. 2019; Strawn et al. 2021) and the "low-pressure" O VI scenario presented in Stern et al. (2018), for which cool, photoionized O VI exists beyond the accretion shock. Detailed discussion on the ionization mechanism is beyond the scope of this paper (see Oppenheimer et al. 2016; Rahmati et al. 2016; Wijers et al. 2020).

We use two approaches to select the gas around galaxies while making the column density maps. Our first approach selects only gas within fixed 3D radii of 1, 2, and 3 $r_{\rm vir}$ from each galaxy center. This method excludes gas further away from the galaxy but appearing nearby because of the 2D projection. The second approach selects gas within a fixed LOS velocity difference $|\Delta v_{\rm LOS}|$ from the galaxy systemic velocity.[10] We use $|\Delta v_{\rm LOS}| = 300\,{\rm km\,s^{-1}}$ and $500\,{\rm km\,s^{-1}}$, both of which are commonly adopted in observational analyses to identify absorption systems associated with the target galaxies (e.g., Chen et al. 2010; Werk et al. 2016). On the column density maps, each pixel shows the total gas column summed along the path enclosed by the sphere of a fixed radius or the LOS velocity window. Each pixel has an area of $(1.25\ {\rm pkpc})^2$ or $(0.005\ r_{\rm vir})^2$.

As an illustration, the maps in Figure 2 show the median Mg II (top) and O VI (middle and bottom) column density for the stacks of all star-forming galaxies. For this figure only, individual galaxies are projected edge-on ($i = 90°$, left) or face-on ($i = 0°$, right) before they are stacked together. The O VI gas clearly extends to a larger radius than Mg II, which is concentrated within 0.4 $r_{\rm vir}$ around the galaxy center. The O VI and Mg II gas also show different morphologies, for which only Mg II but not O VI shows an axisymmetric structure. We defer the discussion of O VI morphology and its dependence on inclination and azimuthal angles to a future paper (S. Ho et al. 2021, in preparation) and refer readers to Ho et al. (2020) for the Mg II analysis.

3. O VI Column Density and Covering Fraction Measurements

The high O VI incidence rate out to at least 150 pkpc ($\approx r_{\rm vir}$) from $\sim L^*$ star-forming galaxies suggest that O VI extends to this radius or further (Tumlinson et al. 2011). In this section, we use EAGLE to demonstrate how selecting the gas within different fixed LOS separations around the target galaxies (1, 2, and 3 $r_{\rm vir}$) and different LOS velocity windows ($|\Delta v_{\rm LOS}| = 300\,{\rm km\,s^{-1}}$ and $500\,{\rm km\,s^{-1}}$) changes the measurements for O VI column density (Section 3.1) and covering fraction (Section 3.2).

[8] The virial radius $r_{\rm vir}$ is the radius enclosing an average density of $\Delta_{\rm vir}\rho_c(z)$, where $\rho_c(z)$ represents the critical density at redshift z. The overdensity $\Delta_{\rm vir}$ follows the top-hat spherical collapse calculation in Bryan & Norman (1998). The halo virial mass is the total mass enclosed within the sphere of radius $r_{\rm vir}$.

[9] Ploeckinger & Schaye (2020) modified the $z > 3$ UV/X-ray background in Faucher-Giguère (2020) to improve the self-consistency of the treatment of attenuation before H I and He II reionization (their Appendix B). This modification is irrelevant to this work at low redshift.

[10] The galaxy systemic velocity is the mass-weighted velocity of all particles (stars, gas, dark matter, and black hole) associated with the galaxy at the $z = 0.271$ snapshot.

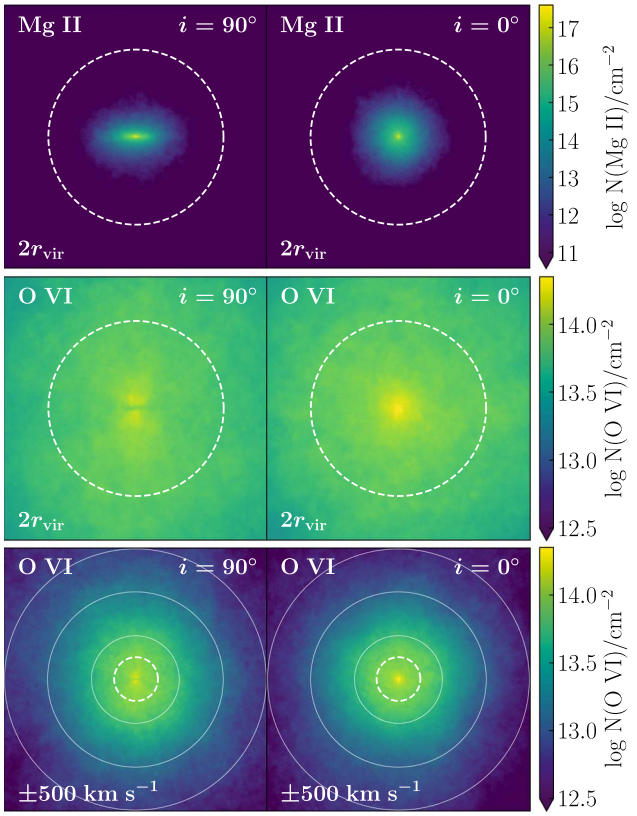

Figure 2. Median Mg II (top) and O VI (middle and bottom) column density around all star-forming central galaxies in the sample. The median stellar mass and halo mass of the stacked galaxies are $10^{9.7}\,M_\odot$ and $10^{11.6}\,M_\odot$, respectively. In the top and middle rows, only the gas within 2 $r_{\rm vir}$ of individual galaxies is included. Each white dashed circle marks a radius of 0.5 $r_{\rm vir}$. The bottom row zooms out and shows the O VI gas distribution at larger scale. The concentric solid circles mark the radii of 1, 2, and 3 $r_{\rm vir}$. The gas around individual galaxies is selected using the LOS velocity window of $|\Delta v_{\rm LOS}| = 500\,{\rm km\,s^{-1}}$. The left and right columns show the edge-on ($i = 90°$) and face-on ($i = 0°$) projections, respectively. The galaxy orientation is defined using the stellar angular momentum vector (as in Ho et al. 2020). The Mg II gas distribution is concentrated near the galaxy center, whereas the O VI gas extends to a larger radius.

3.1. Column Density Profile

We create the column density profiles for stacks of randomly oriented galaxies using all the pixels from individual galaxies in each stack. For the stack of all star-forming galaxies, Figure 3 shows the O VI column density as a function of impact parameter b (left) and that normalized by $r_{\rm vir}$ (right). Each line shows the median column density from gas selected using different criteria.

First, the O VI gas clearly extends beyond $r_{\rm vir}$. The sharp column density drop-off from gas selected within $r_{\rm vir}$ (black) is not observed from gas within 2 $r_{\rm vir}$ (purple) or 3 $r_{\rm vir}$ (magenta). Second, at a fixed impact parameter, gas selected by a larger radius around galaxies produces a higher column density. For impact parameters $b \approx r_{\rm vir}$, the O VI absorption is dominated by gas at ≈ 2 $r_{\rm vir}$ (see also Oppenheimer et al. 2016; Wijers et al. 2020). Although selecting the gas within $2r_{\rm vir}$ and $3r_{\rm vir}$ produces a significantly smaller column density difference compared to that from gas within 1 $r_{\rm vir}$ and larger radii, this still implies a nonnegligible amount of O VI beyond 2 $r_{\rm vir}$. This extended O VI distribution is in stark contrast to the centrally concentrated Mg II distribution (e.g., Figure 2).

More importantly, selecting gas using an LOS velocity window $|\Delta v_{\rm LOS}|$ of $300\,{\rm km\,s^{-1}}$ (orange) or $500\,{\rm km\,s^{-1}}$ (yellow) produces a higher O VI column density at all impact parameters, even compared to that from gas physically within $3r_{\rm vir}$. The difference increases with impact parameter. Consequently, gas selected by $|\Delta v_{\rm LOS}|$ produces a flatter O VI column density profile compared to that from gas within a fixed radius. Altogether, our results imply that even at a small impact parameter ($b < 150$ pkpc or < 1 $r_{\rm vir}$), selecting gas using a fixed LOS velocity window includes a large contribution from O VI that is relatively far away from the galaxies.

Figure 4 shows the median O VI column density profiles for galaxies in different stellar mass bins. The top row shows the profiles from gas physically within 2 $r_{\rm vir}$ (solid lines) and gas selected by the LOS velocity window of $|\Delta v_{\rm LOS}| = 500\,{\rm km\,s^{-1}}$ (dashed lines). Darker (lighter) lines represent the measurements around lower (higher) mass galaxies. In all mass bins, similar to Figure 3, gas within $|\Delta v_{\rm LOS}| = 500\,{\rm km\,s^{-1}}$ produces a higher column density than that from gas within 2 $r_{\rm vir}$ at a fixed impact parameter. To illustrate how the column density difference varies with impact parameter and galaxy stellar mass, the bottom row shows the difference of the median column density profiles. The dashed (dotted) lines show the results from gas within $|\Delta v_{\rm LOS}|$ of $500\,{\rm km\,s^{-1}}$ ($300\,{\rm km\,s^{-1}}$) compared to that from gas inside 2 $r_{\rm vir}$. These plots clearly show that the column density difference increases with impact parameter. Then at a fixed impact parameter, the darker lines generally lie above the lighter lines. This indicates that the difference in the O VI column density is typically larger for a lower-mass galaxy. For example, at $b = 150$ pkpc or ≈ 1 $r_{\rm vir}$, the $9.0 \leqslant \log(M_\star/M_\odot) < 9.5$ galaxies detect a difference of about 0.25 dex, whereas the difference is around 0.1 dex for the $10.0 \leqslant \log(M_\star/M_\odot) < 10.5$ galaxies. In other words, by selecting the gas using the $\pm300\,{\rm km\,s^{-1}}$ or $\pm500\,{\rm km\,s^{-1}}$ window instead of a fixed radius of 2 $r_{\rm vir}$, the measured O VI column density increases by 25%–80% at an impact parameter of 1 $r_{\rm vir}$.

3.2. Covering Fraction

Because selecting gas using a commonly adopted LOS velocity window produces higher O VI column density than that from gas within a fixed radius of $\sim r_{\rm vir}$ around galaxies, gas outside the fixed radius but selected by $|\Delta v_{\rm LOS}|$ will elevate the O VI detection rate for a fixed column density threshold. To illustrate this effect, we calculate the O VI covering fraction as a function of impact parameter. First, we bin the pixels of all galaxies in each stack by the impact parameter b or $b/r_{\rm vir}$. Then, in each bin, we count the number of pixels with O VI column density above the threshold and divide that number by the total number of pixels in the bin.

Figure 5 shows the O VI covering fraction for star-forming galaxies in different stellar mass bins (columns). The top and bottom rows show the fraction as a function of b and $b/r_{\rm vir}$, respectively. We adopt a detection threshold of $\log {\rm N(O\,VI)/cm^{-2}} = 13.5$, which is comparable to the lowest O VI column density detected in quasar sightlines around low-redshift galaxies (e.g., Tumlinson et al. 2011; Johnson et al. 2015). In all mass bins, selecting gas within $|\Delta v_{\rm LOS}| = 500\,{\rm km\,s^{-1}}$ (green dashed lines) and $300\,{\rm km\,s^{-1}}$ (red dotted lines) produces comparable covering fractions with a difference no greater than 0.03. In contrast, selecting gas using either value of $|\Delta v_{\rm LOS}|$ produces a higher covering fraction than gas

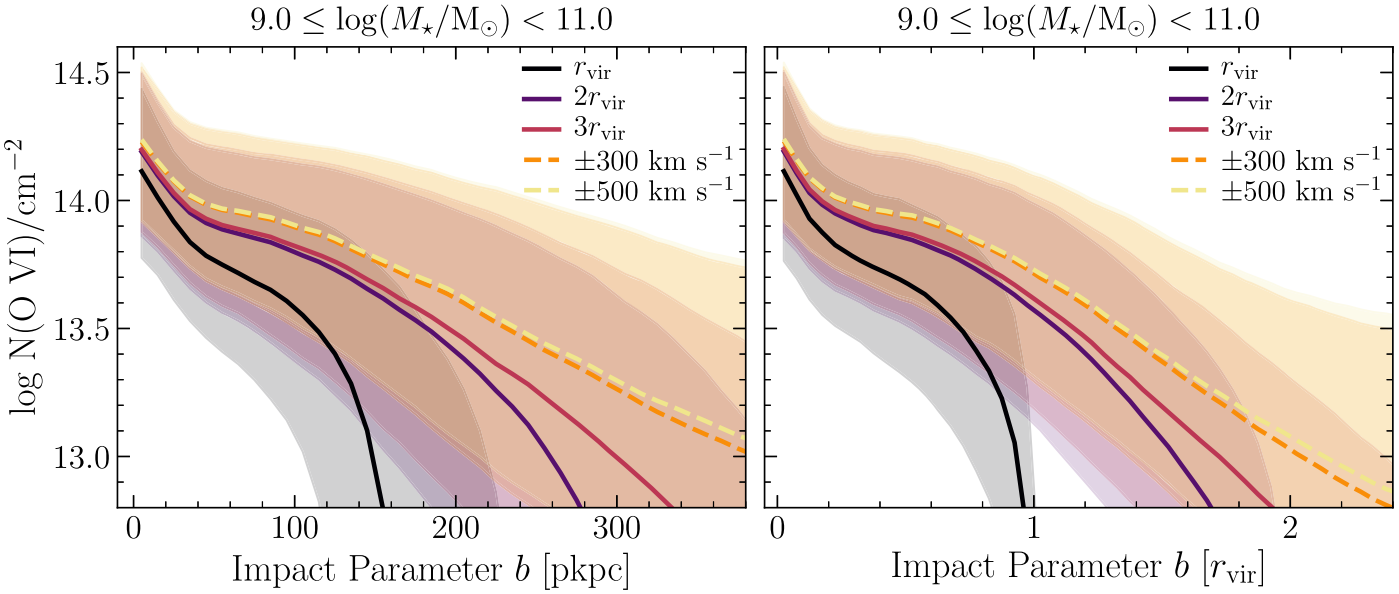

Figure 3. O VI column density as a function of impact parameter (left) and that normalized by halo virial radius (right). Different colors show the column density measured from the gas within 1, 2, or 3 $r_{\rm vir}$ of individual galaxies or within an LOS velocity window of ±300 km s^{-1} or ±500 km s^{-1} from the galaxy systemic velocity. Each line shows the median from all pixels around all star-forming galaxies, and each shaded region of the same color encloses the 16th and 84th percentiles. At all impact parameters, selecting gas using a fixed LOS velocity window produces a higher column density and a flatter column density profile compared to that from gas even within 3 $r_{\rm vir}$.

within 1 $r_{\rm vir}$ or $2r_{\rm vir}$, and the difference is more prominent at larger impact parameters and for lower-mass galaxies. For instance, at $b = 1$ $r_{\rm vir}$ (vertical dotted lines), selecting the gas using 1 $r_{\rm vir}$ produces a zero covering fraction (by definition),[11] but the fraction is clearly above zero when we adopt other selection criteria. If we select the gas using $|\Delta v_{\rm LOS}|$ instead of 2 $r_{\rm vir}$, then the O VI covering fraction around $9 \leqslant \log(M_\star/M_\odot) < 9.5$ ($10 \leqslant \log(M_\star/M_\odot) < 10.5$) galaxies increases from 0.3 to 0.55 (0.75 to 0.85), implying an ≈85% (15%) increase.

4. Discussion and Conclusion

In the past decade, the ubiquitous O VI absorption detected around $\sim L^*$ star-forming galaxies out to a large impact parameter of $\gtrsim 150$ pkpc has generated interest in CGM studies. A challenge for understanding and interpreting circumgalactic absorption is that the measurements do not reveal where the detected gas lies along the LOS. Hence, observers typically identify absorption systems associated with the target galaxies using an LOS velocity cut around the galaxy systemic velocity (e.g., ±300 km s^{-1} and ±500 km s^{-1}). In this paper, we used the high-resolution EAGLE (25 cMpc)^3 simulation and analyzed the O VI gas around $z \approx 0.25$, star-forming galaxies. We demonstrated that the O VI column density and detection rate depend on whether we include gas around galaxies within a fixed 3D radius (1, 2, and 3 $r_{\rm vir}$) or gas selected using an LOS velocity window.

We showed that selecting gas using the commonly adopted LOS velocity windows of $|\Delta v_{\rm LOS}| = 300$ km s^{-1} or 500 km s^{-1} always produces a higher O VI column density and a flatter column density profile compared to gas within a fixed radius (Figure 3). The column density discrepancy increases with impact parameter and generally worsens for lower-mass galaxies (Figure 4). For example, when we compared the column density measured from gas within $|\Delta v_{\rm LOS}|$ and 2 $r_{\rm vir}$, the difference increases from 0.2 dex (0.1 dex) at 1 $r_{\rm vir}$ to over 0.75 dex (0.7 dex) at ≈ 2 $r_{\rm vir}$ for $9.0 \leqslant \log(M_\star/M_\odot) < 9.5$ ($10.0 \leqslant \log(M_\star/M_\odot) < 10.5$) galaxies. Because selecting gas using the $|\Delta v_{\rm LOS}|$ criterion increases the measured O VI column density, it also raises the O VI detection rate for a fixed detection threshold, i.e., the covering fraction (Figure 5).

4.1. Examples of How the Enhanced O VI Column Density Affects the Interpretation of Observational Measurements

We use the COS-Halos data set (Tumlinson et al. 2011) to demonstrate how the elevated O VI column density from the LOS velocity selection affects the O VI mass estimation deduced from observational data. Their sample consists of 30 (12) sightlines within $b = 150$ pkpc, i.e., $\lesssim r_{\rm vir}$, of $z \approx 0.2$, $\sim L^*$ star-forming (quiescent) galaxies, and 27 (4) of the sightlines have detected O VI. By projecting a circular region of radius $R = 150$ pkpc on the sky, they estimated the total mass of O VI around star-forming galaxies using $M_{\rm O\,VI} = \pi R^2 m_{\rm O} \kappa \langle N_{\rm O\,VI} \rangle$, where $m_{\rm O}$ is the oxygen atomic mass, $\langle N_{\rm O\,VI} \rangle$ is the mean O VI column density, and κ is the covering fraction. They measured the $\log \langle N_{\rm O\,VI} \rangle / {\rm cm}^{-2}$ as 14.7, 14.6, and 14.5 in radial bins R of 0–50 pkpc, 50–100 pkpc, and 100–150 pkpc, respectively, but they adopted $\log \langle N_{\rm O\,VI} \rangle / {\rm cm}^{-2} = 14.5$ to obtain an O VI mass lower limit.[12] The resultant O VI and oxygen mass are $2.4 \times 10^6 M_\odot$ and $1.2 \times 10^7 (0.2/f_{\rm O\,VI})$ $M_\odot$, respectively, where $f_{\rm O\,VI}$ is the O VI ionization fraction. Because their sightlines lie within 150 pkpc, this calculation is often interpreted as the total O VI and

[11] In the top row of Figure 5, gas selected within 1 $r_{\rm vir}$ (dotted–dashed curves) does not produce a zero covering fraction at the vertical dotted lines, because the vertical dotted lines only show the median $r_{\rm vir}$ of galaxies in individual mass bins.

[12] Adopting $\log \langle N_{\rm O\,VI} \rangle / {\rm cm}^{-2} = 14.5$ also avoids the calculated O VI and oxygen masses being skewed by sightlines with large log N(O VI) at small impact parameters.

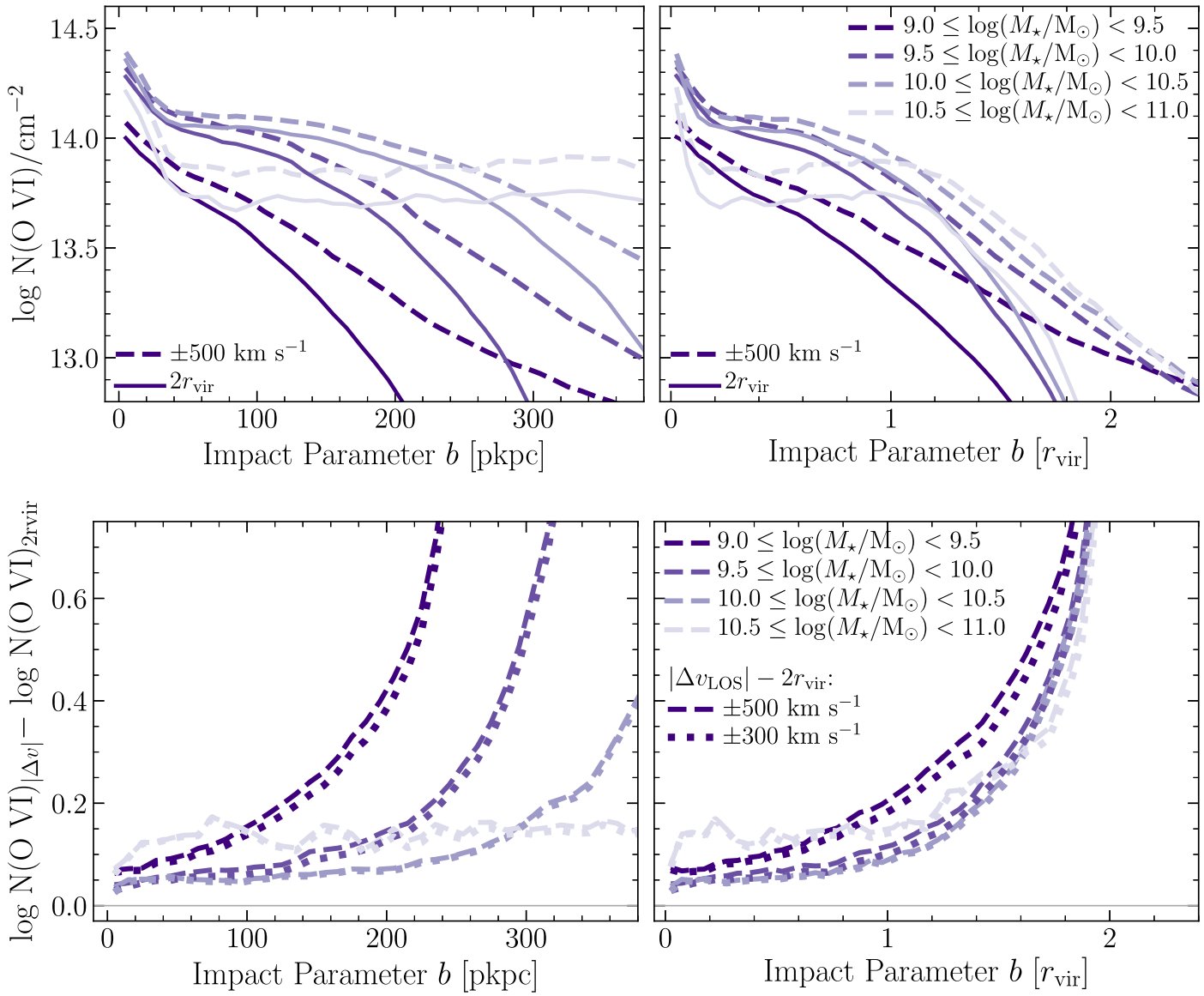

Figure 4. Median O VI column density around star-forming galaxies in different stellar mass bins as a function of impact parameter (left) and that normalized by halo virial radius (right). The top row shows the O VI column density profiles from gas inside 2 $r_{\rm vir}$ (solid lines) and gas selected by an LOS velocity window of $|\Delta v_{\rm LOS}| = 500$ km s^{-1} (dashed lines). The bottom row shows the difference in the median O VI column density profiles between gas selected using $|\Delta v_{\rm LOS}|$ and gas within 2 $r_{\rm vir}$. The dashed (dotted) lines represent the results from $|\Delta v_{\rm LOS}| = 500$ km s^{-1} (300 km s^{-1}). In all panels, darker (lighter) lines show the results for galaxies in the lower (higher) mass bins. In all mass bins, gas within $|\Delta v_{\rm LOS}|$ produces a higher O VI column density than that from gas within 2 $r_{\rm vir}$, and the difference increases with impact parameter.

oxygen mass within a volume of $R < 150$ pkpc, i.e., $\lesssim r_{\rm vir}$, of the star-forming galaxies.

However, our analysis with EAGLE demonstrates that the LOS velocity window selects a nonnegligible amount of O VI gas outside $r_{\rm vir}$. Hence, we use the difference in O VI column density measured from gas within $r_{\rm vir}$ and $|\Delta v_{\rm LOS}|$ to correct the observed log N(O VI) values and recalculate the O VI mass within $r_{\rm vir}$ of the star-forming galaxies. Because Tumlinson et al. (2011) showed that most O VI velocity components have Doppler shifts below ± 300 km s^{-1}, we correct the observed column densities from $|\Delta v_{\rm LOS}|$ of 300 km s^{-1} to within $r_{\rm vir}$ based on the stellar mass of each galaxy and the sightline impact parameter. We note that our calculations and conclusions remain unchanged if we use $|\Delta v_{\rm LOS}| = 200$ km s^{-1} instead (as further discussed in Section 4.2). Figure 6 is analogous to the top row of Figure 4, but the O VI column density profiles are measured from gas within $r_{\rm vir}$ (solid) and $|\Delta v_{\rm LOS}| = 300$ km s^{-1} (dotted) around EAGLE star-forming galaxies. For the 27 observed sightlines with O VI detected in Tumlinson et al. (2011), the average log N(O VI) correction is −0.28 dex, and the corrected $\log\langle N_{\rm O\,VI}\rangle/{\rm cm}^{-2}$ in 0–50 pkpc, 50–100 pkpc, and 100–150 pkpc are 14.47, 14.33, and 14.13, respectively. Following Tumlinson et al., we calculate the mass lower limit using the smallest $\log\langle N_{\rm O\,VI}\rangle$. The 0.37 dex decrease in $\log\langle N_{\rm O\,VI}\rangle/{\rm cm}^{-2}$ (from 14.5 to 14.13) corresponds to a decrease of 57% for the O VI and oxygen masses. Hence, this reduces the baryon budget estimated for the warm-hot CGM by more than 50%.

Detailed discussion of the rare O VI detection around quiescent galaxies and the "O VI bimodality" in the COS-Halos sample is beyond the scope of this paper. However, it is worth noting that Oppenheimer et al. (2016) suggested that this "bimodality" does not imply a causal link between sSFR and O VI column density but reflects the higher halo mass of the quiescent galaxy sample. In fact, even with our

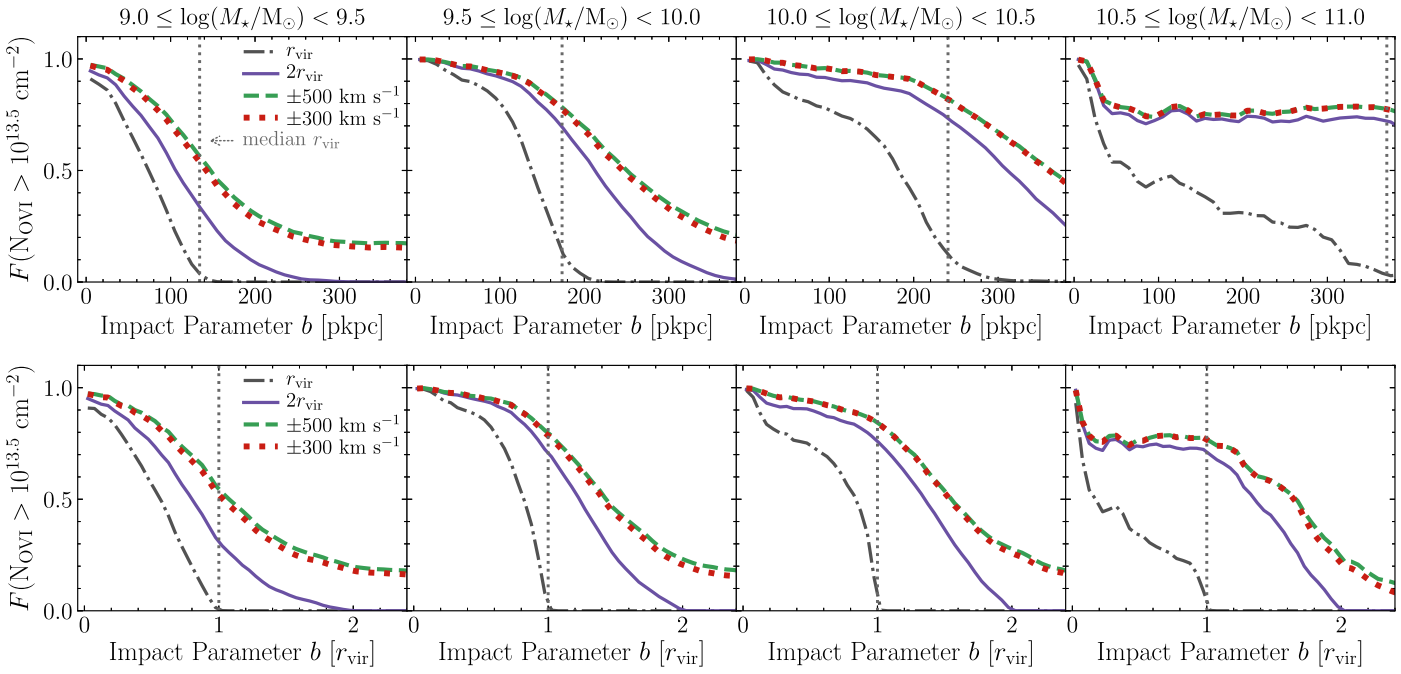

Figure 5. O VI covering fraction for star-forming galaxies as a function of impact parameter (top) and that normalized by the halo virial radius (bottom). The adopted detection threshold is log N(O VI)/cm^{-2} = 13.5. Different columns show the results for galaxies in different stellar mass bins, and different line styles show the results from gas selected using different criteria. The vertical dotted lines show the median $r_{\rm vir}$ of the galaxies in the sample. At a fixed impact parameter, gas selected by $|\Delta v_{\rm LOS}|$ always produces a higher covering fraction than gas within 2 $r_{\rm vir}$, and lower-mass galaxies show a larger difference.

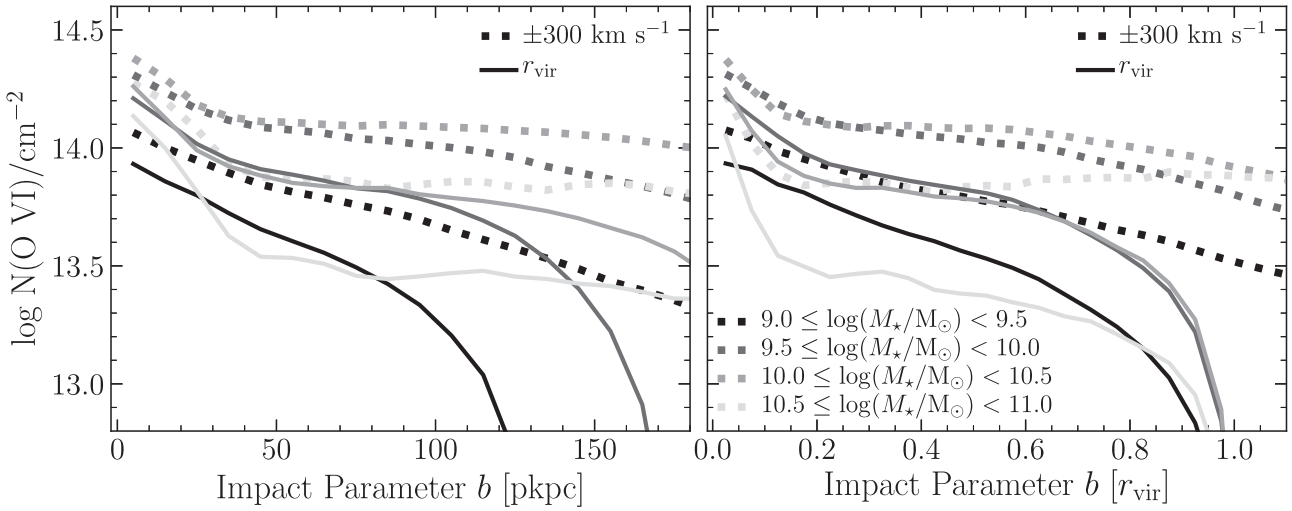

Figure 6. Median O VI column density around star-forming galaxies in different stellar mass bins as a function of impact parameter (left) and that normalized by halo virial radius (right). This figure is analogous to the top row of Figure 4, but this figure shows the profiles measured from gas within $r_{\rm vir}$ (solid lines) and the LOS velocity window of $|\Delta v_{\rm LOS}| = 300$ km s^{-1} (dotted lines). Such selections are comparable to the COS-Halos data set in Tumlinson et al. (2011); the sightlines lie within 150 pkpc ($\lesssim r_{\rm vir}$) of the selected galaxies, and the Doppler shifts of most O VI velocity components lie within ±300 km s^{-1} of the galaxy systemic velocities.

simulated star-forming galaxies only, those with halo masses above $10^{12.5}$ $M_\odot$ have a lower log N(O VI) than those that are slightly less massive. As an illustration, Figure 7 shows the O VI column density as a function of halo mass at fixed impact parameters of 50 pkpc (top) and 150 pkpc (bottom). Different markers represent the results from gas selected using different criteria. Regardless of the selection method we use, galaxies with halo mass above $10^{12.5}$ $M_\odot$ have lower O VI column densities than those around lower-mass halos of $10^{11.5-12.5}$ $M_\odot$. This also agrees with the halo mass dependence of the O VI column density shown in Wijers et al. (2020); low-redshift EAGLE galaxies with halo masses of $\sim 10^{12}$ $M_\odot$ have the highest O VI column density compared to both higher- and lower-mass halos (see their Figure 8). Altogether, this demonstrates the decline of O VI column density at the high-mass end as emphasized in Oppenheimer et al. (2016) while interpreting the COS-Halos measurements.

As another example for the O VI mass calculation, we use the Johnson et al. (2017) sample of 18 star-forming dwarf galaxies with stellar masses of $\sim 10^{8-9}$ $M_\odot$. The authors estimated the O VI mass within $r_{\rm vir} = 90$ pkpc using the mean O VI column density measured from the two sightlines at the smallest impact parameters; these two sightlines detected O VI of log N(O VI)/cm^{-2} = 14.10 and 14.17 at 0.23 $r_{\rm vir}$ and 0.26 $r_{\rm vir}$, respectively. Because our analysis did not include EAGLE galaxies with stellar masses below 10^9 $M_\odot$, we estimate the

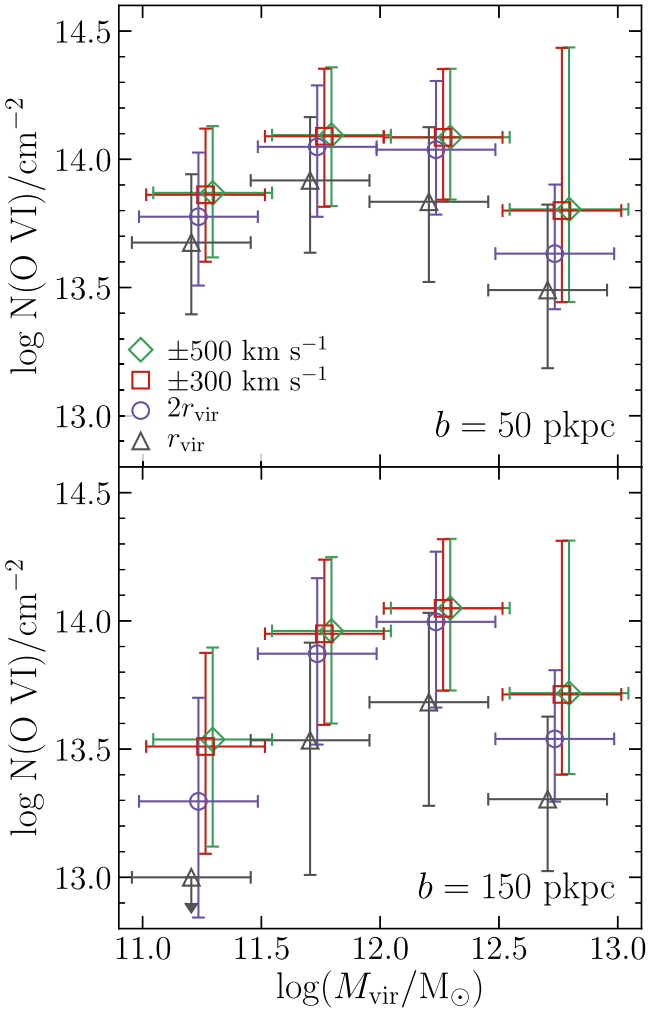

Figure 7. O VI column density around star-forming galaxies as a function of halo mass at impact parameters of 50 pkpc (top) and 150 pkpc (bottom). Different markers show the median O VI column densities measured from gas selected using different criteria. The error bars show the 16th and 84th percentiles. Points are offset along the horizontal axis to avoid the overlapping of error bars. At b = 150 pkpc, the median O VI column density of galaxies with halo masses of $10^{11.0-11.5}$ $M_\odot$ is below the axis limit (downward arrow). Galaxies with halo masses above $10^{12.5}$ $M_\odot$ have a lower O VI column density than those with halo masses of $10^{11.5-12.5}$ $M_\odot$. In all mass bins, gas within $r_{\rm vir}$ always produces a lower O VI column density compared to gas selected by the LOS velocity windows.

column density correction using the results from the EAGLE galaxies with the closest stellar masses ($10^{9-9.5}$ $M_\odot$). The estimated correction is conservative; the column density discrepancy measured from gas within a fixed radius and an LOS velocity window worsens with decreasing stellar mass (Figures 4 and 6). The log N(O VI) correction from $|\Delta v_{\rm LOS}|$ = 300 km s^{-1} to $r_{\rm vir}$ for the two sightlines are −0.16 dex and −0.17 dex. As a result, the mean log N(O VI), and hence the estimated O VI mass, decreases by over 30%.[13]

[13] We obtain a smaller O VI mass correction for the dwarf galaxy sample in Johnson et al. (2017) than the $\sim L^*$ galaxy sample in Tumlinson et al. (2011). This is because Johnson et al. (2017) obtained $\log\langle N_{\rm O\,VI}\rangle$ from sightlines at small impact parameters of 0.23 $r_{\rm vir}$ and 0.26 $r_{\rm vir}$, whereas Tumlinson et al. (2011) used sightlines at larger impact parameters of $b \lesssim 150$ pkpc, i.e., $\lesssim r_{\rm vir}$. However, we note that the correction estimated for the Johnson et al. sample is conservative, because we estimate the correction from EAGLE galaxies an order of magnitude more massive than the observed dwarf galaxies.

Because O VI column density scales with the O VI mass, the difference in O VI column density between gas selected using a fixed radius versus an LOS velocity window demonstrates the difference in the O VI mass included. Even at small impact parameters, when observers use an LOS velocity window to identify the O VI gas associated with the target galaxies, a nonnegligible amount, possibly even a dominant amount of the detected O VI, actually resides at large physical distances (e.g., $>r_{\rm vir}$; Figures 6 and 7). Not only does the gas at large distances increase the O VI detection rate and column density, this gas potentially weakens any O VI kinematic signature produced by gas close to the galaxy. While we defer the O VI kinematic analysis to a future paper (S. Ho et al. 2021, in preparation), a similar analysis of Mg II showed that even though the Mg II gas corotates with galaxies out to at least 0.5 $r_{\rm vir}$, the gas far away ($>$ $r_{\rm vir}$) but selected by the LOS velocity window makes observers less likely to conclude that gas at $\gtrsim$0.25 $r_{\rm vir}$ is corotating (Ho et al. 2020). This result from Mg II illustrates that gas at large distances can "contaminate" the measurements and mask the "true" circumgalactic gas properties.

4.2. Comments on the Radial Extent of O VI Gas and the Small LOS Velocity Differences

While observers typically adopt the ±300 km s^{-1} or ±500 km s^{-1} window to search for absorption systems associated with the target galaxies, most detected O VI systems have Doppler shifts within ±200 km s^{-1} from the galaxy systemic velocity (Tumlinson et al. 2011; Zahedy et al. 2019, private communication). This however is also true for simulations, and when we repeat our analysis with the narrower window of ±200 km s^{-1}, our conclusions remain unchanged. Figure 8 illustrates this point; in particular at small impact parameters ($\lesssim$150 pkpc or $r_{\rm vir}$), the O VI column density profiles measured from gas within ±200 km s^{-1} (red dashed), ±300 km s^{-1} (orange dashed), and ±500 km s^{-1} (yellow dashed) largely overlap. This implies that even out to larger scale, i.e., beyond 1–3 $r_{\rm vir}$ of the galaxies and into the intergalactic scale, the O VI gas still has a small LOS velocity relative to the galaxies.

Figure 8 shows that in order to measure an O VI column density comparable to that from gas selected by the LOS velocity windows of ±300 km s^{-1} (orange dashed) and ±500 km s^{-1} (yellow dashed), we have to include the gas within 30 $r_{\rm vir}$ (light green solid) around the galaxies. In fact, nearly 100% of the O VI gas within 30 $r_{\rm vir}$ have LOS velocities within ±300 km s^{-1} and ±500 km s^{-1} (not shown). Given that the median $r_{\rm vir}$ of our galaxy sample is 160 pkpc; 30 $r_{\rm vir}$ corresponds to about 4.8 pMpc and a Hubble flow velocity of 380 km s^{-1}. This figure clearly demonstrates that O VI extends far beyond 1–3 $r_{\rm vir}$ and to tens of $r_{\rm vir}$ at ∼pMpc scale. The Hubble flow velocity of 380 km s^{-1} also explains why the gas at such a large LOS separation is still included in our velocity windows; unless the O VI resides in massive clusters with peculiar velocities of ∼1000 km s^{-1}, the O VI at ∼pMpc scale moving with the Hubble flow will have LOS velocity comparable to or smaller than ±300 km s^{-1} and ±500 km s^{-1}.

The large spatial extent of O VI gas around galaxies and the small O VI velocity along LOS agree with results from previous observational (and simulation) O VI–galaxy cross-correlation analyses. Prochaska et al. (2019) used the CASBaH survey with thousands of $0.12 < z < 0.75$ galaxies in nine quasar fields and showed that while the O VI covering fraction

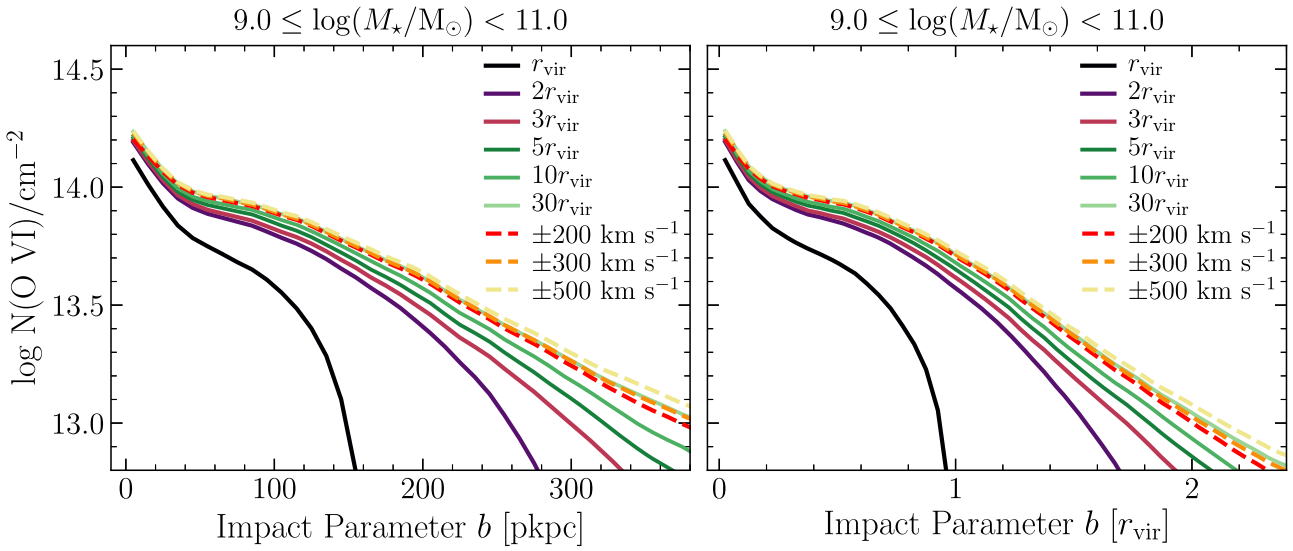

Figure 8. Median O VI column density as a function of impact parameter (left) and that normalized by halo virial radius (right). This figure is similar to Figure 3, but with additional column density profiles measured from gas within 5, 10, and 30 $r_{\rm vir}$ of individual galaxies (greenish solid) and within a LOS velocity window of ±200 km s^{-1} (red dashed) from the galaxy systemic velocity. Gas within 30 $r_{\rm vir}$ (light green solid) of individual galaxies has to be included to produce a median O VI column density profile comparable to those measured from gas selected by the LOS velocity window of ±200 km s^{-1}, ±300 km s^{-1}, or ±500 km s^{-1}.

($\geqslant 10^{13.5}$ cm^{-2}) declines with impact parameter, there still exists an excess in the covering fraction out to ≈ 8 pMpc compared to the expectation from random O VI incidence.[14] This implies an O VI–galaxy clustering out to this length scale, and hence, it is not surprising that we find O VI around galaxies out to a similar scale. With an observed sample of 160 O VI absorbers and over 50,000 galaxies at $z < 1$ and with EAGLE, Finn et al. (2016) showed that O VI has a very small velocity dispersion of $\lesssim 100$ km s^{-1} on ∼pMpc scale. They also measured a lower correlation amplitude in the O VI–galaxy cross-correlation function than that from the galaxy autocorrelation function. They concluded that this potentially implies that O VI and galaxies do not trace the same underlying matter distribution, and not all detected O VI is close to the galaxies. In fact, with the FIRE-2 cosmological simulations, Hafen et al. (2020) showed that especially for low-mass galaxies, most of the CGM at $z = 2$ is accreted onto galaxies but ended up being ejected to the intergalactic medium by $z = 0$. This picture implies the transport of metals to the intergalactic scale at low redshift. Altogether, these results indicate the possibility that a nonnegligible amount of detected O VI traces the warm-hot intergalactic medium (WHIM) beyond the galaxy and group halo scales. The small velocity dispersion and LOS velocity also imply a lack of substantial large-scale O VI inflow and outflow at ∼pMpc scale, which thereby suggest an early chemical enrichment history of the WHIM (e.g., Wiersma et al. 2010; see Finn et al. 2016 for further discussion).

4.3. Caveat on Identifying Circumgalactic Gas in Observational Analysis and the O VI Comparison with Simulations

Our results highlight the challenges and limitations for observers to interpret circumgalactic absorption measurements. Figure 7 clearly shows that the gas within $r_{\rm vir}$ always produces a lower O VI column density compared to gas selected by the LOS velocity windows of ±300 km s^{-1} and ±500 km s^{-1}. Even though the two velocity windows produce indistinguishable O VI column density measurements, this does not imply the gas lies close to ($<r_{\rm vir}$) and/or is bound to the galaxies (see also Figures 3 and 4). In other words, even if different O VI velocity components within the $|\Delta v_{\rm LOS}|$ window have comparable LOS velocities, the detected gas possibly comes from distinct regions and has different physical origins. These velocity components may even be blended and indistinguishable depending on the LOS velocity separation and the resolution of the absorption spectrum. This potentially also explains why O VI does not always have matching velocity components with the centrally concentrated LIS gas (e.g., Werk et al. 2016). Hence, the lack of knowledge of where the gas lies along the LOS makes it challenging for observers to interpret the O VI measurements and deduce the origin(s) of the detected O VI gas.

Our analysis demonstrates a caveat for comparing O VI measurements between observations and simulations. With simulations, the column density is typically calculated by integrating the gas along a column with a specified path length (Hummels et al. 2013; Oppenheimer et al. 2016, etc.). In other words, the gas is selected based on its 3D position relative to the galaxy. This approach is different from observational analyses, which identify the gas based on the LOS velocity regardless of the 3D location.

By selecting the gas around galaxies using the LOS velocity windows, we still underpredict the O VI column density compared to that observed around $\sim L^*$ star-forming galaxies with $10^{14.5}$ cm^{-2} at $b \lesssim 150$ pkpc (Tumlinson et al. 2011). However, the difference we find between velocity and LOS distance selection partially accounts for the differences that have been reported between simulations and observations and thereby reduces the discrepancies reported between the two. Therefore, our analysis emphasizes the importance of recognizing how the use of different criteria for identifying the circumgalactic gas can lead to discrepancies in O VI measurements between observations and cosmological simulations. Zoom-in simulations may not also have a large enough volume

[14] The rate of random O VI incidence is estimated by surveying many sightlines in blind surveys and calculating the number of O VI absorbers per redshift interval.

to include all the gas within the velocity window and may thereby underestimate the projection effects.

We thank the referee for the detailed and thoughtful comments that improved the manuscript. We also thank Hsiao-Wen Chen, Fakhri Zahedy, and Tom Cooper for insightful discussions. This work is partly funded by Vici grant 639.043.409 from the Dutch Research Council (NWO) and is partly supported by the National Science Foundation under AST-1817125. This work used the DiRAC@Durham facility managed by the Institute for Computational Cosmology on behalf of the STFC DiRAC HPC Facility (www.dirac.ac.uk). The equipment was funded by BEIS capital funding via STFC capital grants ST/K00042X/1, ST/P002293/1, ST/R002371/1 and ST/S002502/1, Durham University and STFC operations grant ST/R000832/1. DiRAC is part of the National e-Infrastructure.

ORCID iDs

Stephanie H. Ho https://orcid.org/0000-0002-9607-7365
Crystal L. Martin https://orcid.org/0000-0001-9189-7818
Joop Schaye https://orcid.org/0000-0002-0668-5560

References

Appleby, S., Davé, R., Sorini, D., Storey-Fisher, K., & Smith, B. 2021, MNRAS, 507, 2383
Bahé, Y. M., Crain, R. A., Kauffmann, G., et al. 2016, MNRAS, 456, 1115
Beckett, A., Morris, S., Fumagalli, M., et al. 2021, MNRAS, 506, 2574
Bertone, S., Schaye, J., Booth, C. M., et al. 2010a, MNRAS, 408, 1120
Bertone, S., Schaye, J., Dalla Vecchia, C., et al. 2010b, MNRAS, 407, 544
Bryan, G. L., & Norman, M. L. 1998, ApJ, 495, 80
Chen, H.-W., Helsby, J. E., Gauthier, J.-R., et al. 2010, ApJ, 714, 1521
Crain, R. A., Bahé, Y. M., Lagos, C. D. P., et al. 2017, MNRAS, 464, 4204
Crain, R. A., Schaye, J., Bower, R. G., et al. 2015, MNRAS, 450, 1937
Davies, J. J., Crain, R. A., Oppenheimer, B. D., & Schaye, J. 2020, MNRAS, 491, 4462
Dolag, K., Borgani, S., Murante, G., & Springel, V. 2009, MNRAS, 399, 497
Faucher-Giguère, C.-A. 2020, MNRAS, 493, 1614
Finn, C. W., Morris, S. L., Tejos, N., et al. 2016, MNRAS, 460, 590
Ford, A. B., Werk, J. K., Davé, R., et al. 2016, MNRAS, 459, 1745
Furlong, M., Bower, R. G., Crain, R. A., et al. 2017, MNRAS, 465, 722
Furlong, M., Bower, R. G., Theuns, T., et al. 2015, MNRAS, 450, 4486
Gutcke, T. A., Stinson, G. S., Macciò, A. V., Wang, L., & Dutton, A. A. 2017, MNRAS, 464, 2796
Haardt, F., & Madau, P. 2001, in 35th Rencontres de Moriond, Clusters of Galaxies and the High Redshift Universe Observed in X-Rays, ed. D. M. Neumann & J. T. V. Tran, 64
Hafen, Z., Faucher-Giguère, C.-A., Anglés-Alcázar, D., et al. 2020, MNRAS, 494, 3581
Ho, S. H., & Martin, C. L. 2020, ApJ, 888, 14
Ho, S. H., Martin, C. L., Kacprzak, G. G., & Churchill, C. W. 2017, ApJ, 835, 267
Ho, S. H., Martin, C. L., & Schaye, J. 2020, ApJ, 904, 76
Huang, Y.-H., Chen, H.-W., Shectman, S. A., et al. 2021, MNRAS, 502, 4743
Hummels, C. B., Bryan, G. L., Smith, B. D., & Turk, M. J. 2013, MNRAS, 430, 1548
Ji, S., Chan, T. K., Hummels, C. B., et al. 2020, MNRAS, 496, 4221
Johnson, S. D., Chen, H.-W., & Mulchaey, J. S. 2015, MNRAS, 449, 3263
Johnson, S. D., Chen, H.-W., Mulchaey, J. S., Schaye, J., & Straka, L. A. 2017, ApJL, 850, L10
Kacprzak, G. G., Churchill, C. W., & Nielsen, N. M. 2012, ApJL, 760, L7
Kacprzak, G. G., Vander Vliet, J. R., Nielsen, N. M., et al. 2019, ApJ, 870, 137
Lagos, C. d. P., Crain, R. A., Schaye, J., et al. 2015, MNRAS, 452, 3815
Marra, R., Churchill, C. W., Kacprzak, G. G., et al. 2021, ApJ, 907, 8
Martin, C. L., Ho, S. H., Kacprzak, G. G., & Churchill, C. W. 2019, ApJ, 878, 84
McAlpine, S., Helly, J. C., Schaller, M., et al. 2016, A&C, 15, 72
Moustakas, J., Coil, A. L., Aird, J., et al. 2013, ApJ, 767, 50
Nelson, D., Kauffmann, G., Pillepich, A., et al. 2018, MNRAS, 477, 450
Nielsen, N. M., Churchill, C. W., Kacprzak, G. G., Murphy, M. T., & Evans, J. L. 2015, ApJ, 812, 83
Nielsen, N. M., Kacprzak, G. G., Muzahid, S., et al. 2017, ApJ, 834, 148
Oppenheimer, B. D., Crain, R. A., Schaye, J., et al. 2016, MNRAS, 460, 2157
Oppenheimer, B. D., & Schaye, J. 2013, MNRAS, 434, 1063
Oppenheimer, B. D., Schaye, J., Crain, R. A., Werk, J. K., & Richings, A. J. 2018a, MNRAS, 481, 835
Oppenheimer, B. D., Segers, M., Schaye, J., Richings, A. J., & Crain, R. A. 2018b, MNRAS, 474, 4740
Planck Collaboration, Ade, P. A. R., Aghanim, N., et al. 2014, A&A, 571, A16
Ploeckinger, S., & Schaye, J. 2020, MNRAS, 497, 4857
Prochaska, J. X., Burchett, J. N., Tripp, T. M., et al. 2019, ApJS, 243, 24
Prochaska, J. X., Weiner, B., Chen, H. W., Mulchaey, J., & Cooksey, K. 2011, ApJ, 740, 91
Rahmati, A., Schaye, J., Bower, R. G., et al. 2015, MNRAS, 452, 2034
Rahmati, A., Schaye, J., Crain, R. A., et al. 2016, MNRAS, 459, 310
Roca-Fàbrega, S., Dekel, A., Faerman, Y., et al. 2019, MNRAS, 484, 3625
Schaller, M., Dalla Vecchia, C., Schaye, J., et al. 2015, MNRAS, 454 2277
Schaye, J., Crain, R. A., Bower, R. G., et al. 2015, MNRAS, 446, 521
Schroetter, I., Bouché, N. F., Zabl, J., et al. 2019, MNRAS, 490, 4368
Springel, V. 2005, MNRAS, 364, 1105
Springel, V., White, S. D. M., Tormen, G., & Kauffmann, G. 2001, MNRAS, 328, 726
Stern, J., Faucher-Giguère, C.-A., Hennawi, J. F., et al. 2018, ApJ, 865, 91
Strawn, C., Roca-Fàbrega, S., Mandelker, N., et al. 2021, MNRAS, 501, 4948
Suresh, J., Rubin, K. H. R., Kannan, R., et al. 2017, MNRAS, 465, 2966
Trayford, J. W., Camps, P., Theuns, T., et al. 2017, MNRAS, 470, 771
Trayford, J. W., Theuns, T., Bower, R. G., et al. 2015, MNRAS, 452 2879
Tumlinson, J., Peeples, M. S., & Werk, J. K. 2017, ARA&A, 55, 389
Tumlinson, J., Thom, C., Werk, J. K., et al. 2011, Sci, 334, 948
Turner, M. L., Schaye, J., Crain, R. A., et al. 2017, MNRAS, 471, 690
Turner, M. L., Schaye, J., Crain, R. A., Theuns, T., & Wendt, M. 2016, MNRAS, 462, 2440
Wendland, H. 1995, Adv. Comput. Math., 4, 389
Werk, J. K., Prochaska, J. X., Cantalupo, S., et al. 2016, ApJ, 833, 54
Wiersma, R. P. C., Schaye, J., Dalla Vecchia, C., et al. 2010, MNRAS, 409, 132
Wiersma, R. P. C., Schaye, J., & Smith, B. D. 2009, MNRAS, 393, 99
Wijers, N. A., Schaye, J., & Oppenheimer, B. D. 2020, MNRAS, 498, 574
Wijers, N. A., Schaye, J., Oppenheimer, B. D., Crain, R. A., & Nicastro, F. 2019, MNRAS, 488, 2947
Zabl, J., Bouché, N. F., Schroetter, I., et al. 2019, MNRAS, 485, 1961
Zahedy, F. S., Chen, H.-W., Johnson, S. D., et al. 2019, MNRAS, 484, 2257